THE JOURNAL OF PHYSICAL CHEMISTRY C

Article

pubs.acs.org/JPCC

Effect of Dopant–Host Ionic Radii Mismatch on Acceptor-Doped Barium Zirconate Microstructure and Proton Conductivity

Elisa Gilardi,[†] Emiliana Fabbri,[‡] Lei Bi,[§] Jennifer L. M. Rupp,[∥] Thomas Lippert,[†,¶] Daniele Pergolesi,*[,†] and Enrico Traversa*[,⊥,#]

[†]Thin Films and Interfaces, Research with Neutrons and Muons Division, Paul Scherrer Institut, 5232 Villigen, PSI, Switzerland

[‡]Electrochemistry Laboratory, Paul Scherrer Institut, 5232 Villigen, Switzerland

[§]Institute of Materials for Energy and Environment, College of Materials Science and Engineering, Qingdao University, Ningxia Road No. 308, Qingdao 266071, China

[∥]Electrochemical Materials Laboratory, Massachusetts Institute of Technology, MIT, 02139 Cambridge, Massachusetts, United States

[¶]Department of Chemistry and Applied Biosciences, Laboratory of Inorganic Chemistry, Vladimir-Prelog-Weg 1-5/10, ETH Zürich, 8093 Zürich, Switzerland

[⊥]International Research Center for Renewable Energy, Xi'an Jiaotong University, Xi'an, Shaanxi 710049, P. R. China

[#]NAST Center & Department of Chemical Science and Technology, University of Rome Tor Vergata, 00133 Rome, Italy

ABSTRACT: In the present study, morphological and electrical properties of $BaZrO_3$ were investigated as a function of the ionic radii mismatch between Zr and the different B-site dopants (Al, Sc, In, Lu, Tm, Y, Gd, Sm, Nd, and La) for the same solute concentration and valence. Our study highlights the critical role of the ionic radius of the acceptor dopant on stability, sinterability, and proton conductivity of barium zirconate. From our study, Gd-doped barium zirconate emerges as a novel promising material for proton conductor electrolytes.

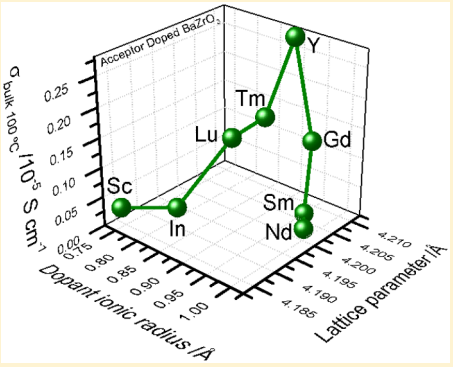

INTRODUCTION

High temperature proton conductors (HTPCs) have received growing interest in the last decades as potential electrolyte materials in intermediate temperature (IT, 400–600 °C) solid oxide fuel cells.[1−3] HTPCs, particularly perovskite-type oxides, show high proton conductivity (larger than 10^{-2} S cm^{-1} at 450 °C) when exposed to hydrogen and/or water vapor containing atmospheres.[4−6]

The substitution of the B^{4+} cation with a trivalent element M^{3+} in the ABO_3 perovskite structure leads to the formation of oxygen-ion vacancies; in the presence of water vapor the water molecule dissociates into a hydroxide ion and a proton: the former fills an oxygen vacancy, while the latter can form a covalent bond with lattice oxygen (dissociative absorption of water).[7−10]

Once protonic defects are incorporated inside the lattice, protons migrate by hopping between adjacent oxygen ions via a Grotthuss-type mechanism.[11]

Doped $BaZrO_3$ (BZ) and $BaCeO_3$ (BC) are up to now the most promising perovskite oxides, but despite their high protonic conductivity many factors limit their practical use; such as the poor sinterability, the low grain boundary conductivity, and the inevitable BaO evaporation during sintering at high temperatures for the former, as well as the low chemical stability in water and CO_2 containing environments for the latter.[12−15]

The effect of different trivalent dopants on the sintering and conductive properties of perovskite oxides has been extensively studied in the past years and in particular the close relation between proton mobility and perovskite structural parameters has attracted much attention.[16−28]

Han et al.[29] studied the relation between the structural properties and the bulk proton conductivity in acceptor-doped BZ and suggested a linear relation between the bulk conductivity and the variation of lattice constant upon hydration. They indicated Tm as the best dopant, while for doping with ionic radii larger than Dy the bulk protonic conductivity drastically decreases.

On the other hand, Gorelov et al.[30] suggested that for doped barium zirconate there is no correlation between the total conductivity and the ionic radius of dopants, reporting a more

Received: March 7, 2017
Revised: April 10, 2017
Published: April 10, 2017

DOI: 10.1021/acs.jpcc.7b02163
J. Phys. Chem. C 2017, 121, 9739−9747

general trend of decreased conductivity in the following order Ho > Sc > Dy, In > Gd.

Additionally, other important factors as the different chemical nature of the cations, as well as the carrier concentration and the trapping effect between protons and dopants have been reported to have a specific influence on proton migration.[7,13,31] In general different correlations between the nature of the dopants and the structural/conducting properties of the perovskite have been suggested.[27,29,30,32−35] In the case of Sc-, In-, Y-, and Gd-doped barium zirconates, the chemical matching in term of basicity and electronegativity for the solute-host was suggested to be the most relevant parameter for the choice of the trivalent dopant since it affects directly the proton mobility. Other parameters as symmetry and lattice constant are instead less critical.[27] In particular, a similar electron density of the oxygen ions coordinated to the Y and to the Zr cations was indicated as one of the main reasons of the unique proton transport properties of Y-doped $BaZrO_3$. The highest proton diffusivity and the lowest activation enthalpy were found for 10 to 20 mol % Y-doped barium zirconate, with tetragonal symmetry. Differently, smaller dopant cations such as Sc lowered the proton mobility, even though the host dopant size mismatch led to smaller cell distortion, allowing the cell to retain the cubic symmetry.

Moreover, for equal dopant content, synthesis method and sintering time, the ionic radius of the dopant has been demonstrated to affect considerably the sintering properties of the samples and thus the microstructure. This in turn affects the protonic transport properties of barium zirconate doped with different trivalent cations.[33] Small cations (Sc and In) led to the formation of relatively large and uniform average grains size; these zirconates showed moderate proton conductivity. In contrast, doping with larger cations (Y, Yb, Tu, Er, Ho) led to the formation of grains with nonuniform and overall smaller average grain sizes showing comparatively higher protonic conductivity. It worth noting that a uniform micromorphology could be achieved increasing the sintering time from 24 to 100 h.[36]

Since structural, chemical and morphological parameters deeply affect the proton conducting properties of doped barium zirconates, this study aims in providing a comprehensive understanding of how these parameters vary as a function of the ionic radii mismatch between Zr and different B-site dopants for equal solute concentration and valence. We contribute to the ongoing debate of the dopant-host lattice mismatch on alteration of protonic conduction and its specific correlation. Despite first studies in the field on microstructural evolution and the implication of dopants acting on grain and grain boundary matrices, still knowledge on sintering and host lattice incorporation of dopants is required. This ultimately affects the ceramic processing approaches to fabricate the next generation proton conducting fuel cells and electrolyzers.

In particular, several trivalent elements in the series Al, Sc, In, Lu, Tm, Y, Gd, Sm, Nd, and La have been substituted in the $BaZrO_3$ lattice and the effects of the dopant on the lattice parameter, sinterability, bulk, specific grain boundary, and total conductivity were investigated.

While in the literature Y is generally identified as the best dopant for $BaZrO_3$, our study unveils that Gd-doped barium zirconate is also a promising protonic conductor.

METHODS

Materials Synthesis. For the synthesis of $BaZr_{0.8}M_{0.2}O_{3-\delta}$ (BZ-M, with M = Al, Sc, In, Lu, Tm, Y, Gd, Sm, Nd, La) $Ba(NO_3)_2$ (99.9%), $ZrO(NO_3)_2{\cdot}2H_2O$ (97%), $Al(NO_3)_3{\cdot}9H_2O$ (99.9%), Sc_2O_3 (99.9%), $In(NO_3)_3{\cdot}6H_2O$, Lu_2O_3 (99.9%), $Tm(NO_3)_3{\cdot}5H_2O$ (99.9%), $Y(NO_3)_3{\cdot}6H_2O$ (99.99%) $Gd(NO_3)_3$ (99.5%), $Sm(NO_3)_3$ (99.5%), $Nd(NO_3)_3$ (99.5%), and La_2O_3 (99.9%) were used as starting materials. Sc_2O_3, Lu_2O_3, and La_2O_3 were first dissolved in a 0.2 M nitric acid solution. $Ba(NO_3)_2$, $ZrO(NO_3)_2$, and $M(NO_3)_3$ were successively dissolved in 200−300 mL of deionized water under continuous stirring at 40 °C to produce transparent metal-nitrate solutions. Citric acid, which is able to bind the metal ions and acts as a fuel in combustion reaction, was then added to the metal-nitrates solution. The molar ratio of citric acid (CA) with respect to the total metal cation (MC) content was set to 1.5 NH_4OH and was added to the solution to adjust the pH value around 8. The transparent aqueous solution containing metal nitrates and citric acid was heated up to 80 °C overnight on a hot plate under stirring. Water vapor gradually evolved with a corresponding increase in viscosity. Finally, the solution was converted to a viscous gel due to thermal dehydration and ignited to a flame, resulting in black ash. The BZ-M powders were calcined under static air at 1100 °C for 6 h to obtain single phase oxides.

Dense BZ-M pellets, 13 mm in diameter and about 1 mm thick, were obtained by uniaxially pressing the powders at 150 MPa for 1 min and subsequently by sintering at 1600 °C for 8 h in air (pellets were covered with powders of the same composition to limit Ba evaporation) with a heating and cooling rate of 5 °C min^{-1}.

For Al, In, Gd, Sm, Nd, and La as dopants the density of the samples was above 94% of the theoretical value. BZY reaches a relative density of 90%, while for M = Sc, Tm, and Lu the relative densities were between 72% and 76%.

Microstructure Characterization. Phase identification of the calcined powders and sintered pellets was carried out using X-ray diffraction (XRD, Rigaku, Ultima III) analysis with Cu K_α radiation using a scanning rate of 2° min^{-1} at room temperature, calibrating the XRD offset using a Si wafer. The pseudocubic lattice parameters were calculated using the MDI Jade program.

The pellet microstructure was observed using a field emission scanning electron microscope (FE-SEM, Hitachi, S-4800). BZ-M compact rectangular bars, with dimensions of 1 mm × 5 mm × 10 mm, were fabricated by uniaxially pressing the ceramic powders at 245 MPa for 1 min. The shrinkage behavior of the green samples was measured from room temperature to 1600 °C with a heating rate of 10 °C min^{-1} using a thermal expansion analyzer (DIL 402C, Netzsch) in flowing air.

Chemical Analysis. The powders and pellet compositions were checked by inductively coupled plasma atomic emission spectroscopy (ICP-AES, Nippon Jarrell-Ash Co., Kyoto, Japan). Experiments were performed at least three times on a sample from the same batch to determine the uncertainty of the concentration of the cations.

Impedance Spectroscopy. For conductivity measurements, two symmetrical porous Pt electrodes were coated onto both sides of polished BZ-M pellets and heated to 1000 °C for 20 min. Impedance spectroscopy (IS) measurements were performed in humidified Ar (ca. 3 vol % H_2O) atmospheres using a multichannel potentiostat VMP3 (Bio-

DOI: 10.1021/acs.jpcc.7b02163
J. Phys. Chem. C 2017, 121, 9739−9747

Logic Co.), in the 0.1 Hz−1 MHz frequency range, with an applied AC voltage amplitude of 100−300 mV. ZView software was used to fit the acquired impedance data to equivalent circuits.

IS measurements, performed in humidified atmosphere between 25 and 700 °C were used to evaluate the conductivity of BZ-M pellets as well as to distinguish the grain interior and the grain boundary contributions. Impedance plot have been fitted with three equivalent circuits connected in series, each equivalent circuit constituted of a resistance and a constant phase element in parallel. The different time constants (τ = RC) of the three circuits enable the separation of the frequency domain in grain-interior (bulk), grain-boundary and electrode contributions. Below 300 °C the complex impedance plane plot of all samples displayed three semicircles, the first one at high-frequencies was assigned to the bulk of BZ-M ceramics. In the case of the most resistive samples (particularly Sm-, Nd-, La-, and Al-doped $BaZrO_3$) the bulk semicircle was already accessible below 400 °C. The second semicircle at intermediate frequencies was assigned to the grain boundary contribution while the third semicircle at low frequencies was instead attributed to the electrode processes. From the analysis of the complex impedance plots bulk, grain boundary and total conductivity were calculated.

Only for BZ-Nd and BZ-Tm the impedance plots were too scattered in the low frequency range to allow a precise estimation of the intercept on the real axis and therefore of the grain boundary resistance, while the bulk semicircle was clearly visible at low temperature in the high frequency range of the plot.

The temperature range used to calculate the activation energy corresponds to the range where the conductivity measurements were performed and it is shown in Figure 7 for all samples.

The specific grain boundary conductivity was calculated according to the brick layer model, under the assumption that the dielectric constants of bulk and grain boundary are very close ($\varepsilon_{bulk} \approx \varepsilon_{g.b.}$), using a single temperature independent $C_{bulk}/C_{g.b.}$ for each sample, as follows:[37]

$$\sigma_{\text{grain boundaries,spec}} = \sigma_b \frac{R_{bulk} C_{bulk}}{R_{g.b.} C_{g.b.}}$$

RESULTS AND DISCUSSIONS

Structural Analysis of BZ-M Powders. Parts a−j of Figure 1 show the X-ray diffraction (XRD) patterns for $BaZr_{0.8}M_{0.2}O_{3-\delta}$ (BZ-M, with M = Al, Sc, In, Lu, Tm, Y, Gd, Sm, Nd, La) powders calcined under static air at 1100 °C for 6 h. Barium zirconate doped with 20 mol % of Al, Sc, In, Lu, Tm, Y, Gd, and Sm shows only the diffraction peaks associated with the cubic perovskite structure (Figure 1a−h), while a clear presence of secondary phases can be observed in the case of doping with the larger cations, namely Nd and La (Figure 1i,j). Figure 1k compares the XRD plots of the different BZ-M compositions in the angular region around the (110) diffraction peak which is the highest intensity peak. The smallest angular position of the (110) diffraction peak, i.e., the largest lattice parameter of the cubic cell, was found for yttrium doping; while for smaller and larger ionic radii of the dopant the angular position of the (110) diffraction peak shifts toward larger 2θ values, indicating a smaller lattice parameter.

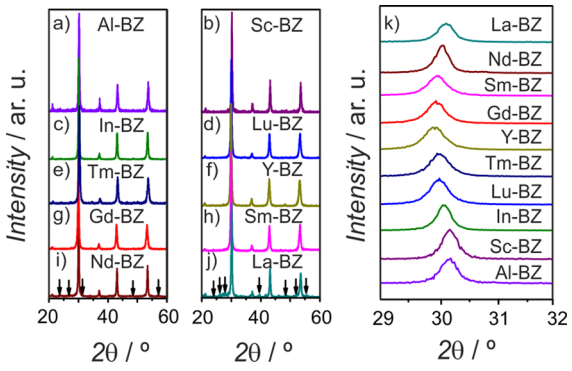

Figure 1. (a−j) XRD patterns of $BaZr_{0.8}M_{0.2}O_{3-\delta}$ (M = Al, Sc, In, Lu, Tu, Y, Gd, Sm, Nd, La) powders. Diffraction peaks belonging to secondary phases are indicated by arrows (i, j). (k) Magnification of the angular region around the (110) diffraction peak of the different compounds.

Figure 2 shows the lattice parameters (pseudocubic symmetry) calculated from the XRD measurements as a function of the dopant ionic radius in octahedral coordination. This highlights the variation of the lattice parameter as a function of the dopant ionic radius, and therefore the structural modifications induced by the dopant to the $BaZrO_3$ cell. Only the BZ-M compositions comprising a cation with an ionic radius ranging between Sc and Y follow Vegard's law. BZ-Al shows a larger lattice parameter than the one expected from the linear relation between lattice parameter of the doped barium zirconate and ionic radius of the dopant. This suggests that Al has been only partially substituted into the barium zirconate lattice. The absence of diffraction peaks from secondary phases indicates that the segregated phase is amorphous.

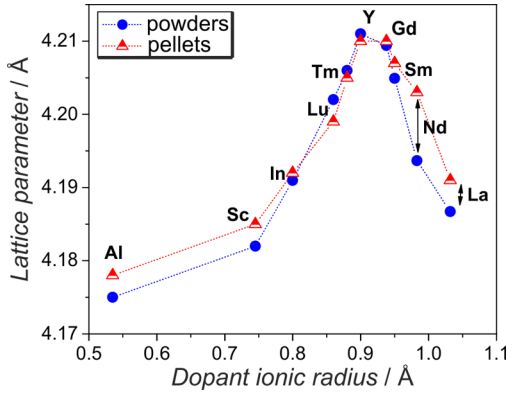

Figure 2. Lattice parameter of BZ-M calculated from the XRD pattern of the powder and pellet plotted as a function of the ionic radius of the dopants.

From Y to La the lattice parameter decreases with increasing the dopant ionic radius. Within the limit of the XRD analysis, no secondary phases were observed for Gd and Sm-doped barium zirconate. The decrease of the lattice parameters may be interpreted as the result of dopant incorporation into the Ba site of the perovskite structure. Since the ionic radius of Ba is 1.61 Å, i.e. larger than the ionic radius of any of the dopants used for this work, the hypothetical substitution of each of the selected dopants into the Ba site would result in a decrease of the lattice parameter. It is reasonable to assume a partial substitution of Gd or Sm cations on the Ba sites, which would

DOI: 10.1021/acs.jpcc.7b02163
J. Phys. Chem. C 2017, 121, 9739−9747

lead to the formation of BaO. As a consequence, oxygen vacancies are consumed instead of being created. This hypothesis is indeed consistent with several experimental and theoretical studies reported in the literature.[7,14,38−42] Haile et al.[39−41] suggested that, particularly for barium cerates, smaller dopant ions are preferentially incorporated into the B site whereas larger ions are incorporated into the A site. In fact, doped barium zirconate remains as a single phase even under 4−10 mol % of Ba deficiency, while undoped perovskites cannot accommodate any alkaline earth deficiencies. Considering the previous observations, the present results for 20 mo % - doped $BaZrO_3$ suggest that for dopant ionic radii larger than Gd a partial substitution of the dopant on the Ba site can occur.

In the specific case of Gd-doped BZ, Gd on Ba site would be in an 8-fold coordination, with an ionic radius of 1.06 Å, thus 34% smaller than barium (here in 12-fold coordination); while in the case of Gd sitting on the Zr site the ionic radius of Gd is 23% larger than that of Zr (both are considered in 6-fold coordination). It is therefore reasonable to assume that a slight substitution of Gd on the Ba site takes place.

It is noteworthy that the difference in lattice parameter of Nd-BZ before and after sintering is significantly larger compared to those measured for all other compositions. This could also be due to the fact that Nd can be stabilized in the oxidation state +4 in $BaZrO_3$, without altering the cubic structure, after heating treatment at high temperature.[43] The lattice parameter here calculated is indeed very close to the value reported on Nd 20% -BZ, where up to the 25% of dopant is oxidized to Nd^{4+}. The smaller ionic radius of Nd^{4+} could favor a redistribution of dopant on the Zr site.[43] In this case, the deriving point defect does not acquire any net charge (Nd_{Zr}^{x}) and no oxygen vacancies are created, thus sensibly reducing the concentration of protonic defects.[44]

Sinterability. Figure 3 reports the XRD patterns of BZ-M pellets sintered at 1600 °C for 8 h. The BZ-Al XRD pattern

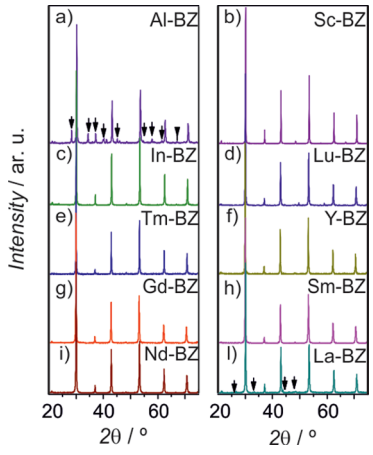

Figure 3. (a−j) XRD patterns of BZ-M pellets sintered at 1600 °C for 8 h. Peaks belonging to secondary phases are indicated by arrows.

(Figure 3a) shows that after the high temperature treatment clearly distinguishable diffraction peaks belonging to a secondary phase are visible.

The sample is composed by two phases: doped $BaZrO_3$ and $Ba_2Al_2O_4$. The fact that these peaks are visible only after sintering suggests the formation of the secondary phase during the heating treatment; $BaAl_2O_4$ can in fact at high temperature by the reaction of Al_2O_3 and $BaCO_3$.[45]

On the other hand, the XRD pattern of BZ-Nd after sintering indicates a single phase perovskite, while before the heating treatment it showed also second phases. This suggests that the second phase was incorporated into the perovskite structure during the heating treatment.

Also, in the XRD pattern of the BZ-La pellet the relative intensity of the peaks related to secondary phases decreases compared to powders (Figure 3 j). These findings suggest that the high temperature sintering facilitates the incorporation into the $BaZrO_3$ lattice of the cations with large ionic radii such as Nd and La.

As reported in Figure 2, no significant differences were found between the powder and pellet lattice parameters for the same composition with the exceptions of Nd- and La-doped barium zirconate. BZ-Nd and BZ-La pellets showed larger lattice parameters than the respective powders; this suggests larger incorporation of the dopant into the lattice after the high temperature treatment, in agreement with the XRD patterns.

Figure 4 shows the temperature dependence of the normalized linear shrinkage (defined as $\Delta l/l_0$, ratio between

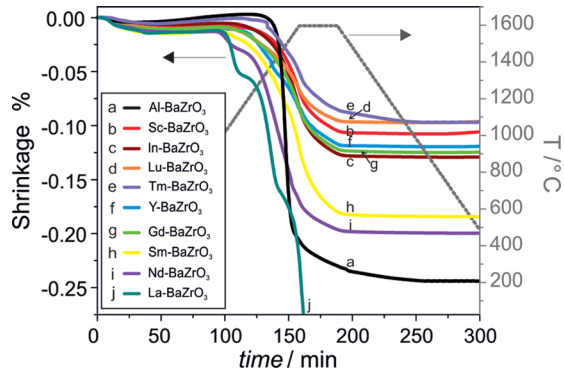

Figure 4. Temperature dependence of the normalized linear shrinkage for not sintered BZ-M pellets.

the sample length variation on the original length), for BZ-M green (not sintered) pellets. The shrinkage of Sm-, Nd-, and La-doped barium zirconate started at about 1000 °C, which is around 300 °C lower than that of the shrinkage onset for all the other dopants. At 1600 °C, the maximum test temperature, the final shrinkage for BZ-Sm, BZ-Nd, and BZ-La was about 17.5%, 20%, and 32%, respectively, while for all other compositions it ranges between 13% for BZ-In to 9.5% for BZ-Lu, which showed the lowest sinterability. These results indicate that doping at 20 mol % with different cations can strongly influence the sinterability of barium zirconate depending on the selected dopant cation.

The influence of the dopant on the sintering properties of barium zirconate was also investigated performing dilatometric measurements and SEM analysis to probe the linear shrinkage upon sintering and the morphology of the sintered pellets.

Scanning electron microscopy (SEM) analysis was used to investigate the microstructure of the BZ-M sintered pellets. Figure 5 shows the SEM images of the BZ-M pellet fractured surfaces after sintering in air at 1600 °C for 8 h. As expected from the dilatometric measurements the good sinterability of Sm-, Nd-, and La-doped barium zirconate compounds was confirmed. The sintered pellets showed dense microstructures, with average grain sizes of 4, 5, and 8 μm, respectively, and well crystallized, polyhedral grains (Figure 5). Among the other compositions, Gd- and In-doped $BaZrO_3$ showed a relatively

DOI: 10.1021/acs.jpcc.7b02163
J. Phys. Chem. C 2017, 121, 9739−9747

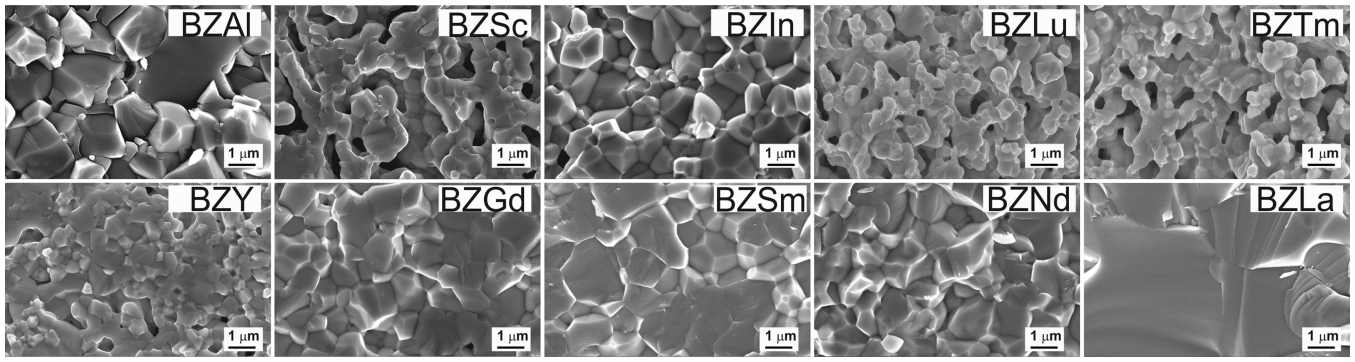

Figure 5. SEM micrographs of BZ-M pellets sintered at 1600 °C for 8 h.

dense microstructure, with an average grain size of 1 μm. BZ-Y showed a more porous microstructure with smaller grain size, and a further decrease of density and grain size was observed for Lu, Sc, and Tm dopants.

The better sinterability of barium zirconate doped with large cations such as Sm, Nd, and La can be explained considering that if the large dopants substitute Ba in the perovskite structure, the segregated barium oxide might form a liquid phase, which would be able to promote the grain growth of barium zirconate during the sintering, as reported for similar compositions.[33] Indeed, as can be seen from Figure 5 in the samples doped with Sm, Nd, and La, no sharp grain boundaries are present, which suggest a different grain boundary composition compared to samples doped with the other cations in the series.

Chemical Composition. The elemental composition for the BZ-M powders and pellets was investigated by inductively coupled plasma analysis. Figure 6 shows the Ba content as a

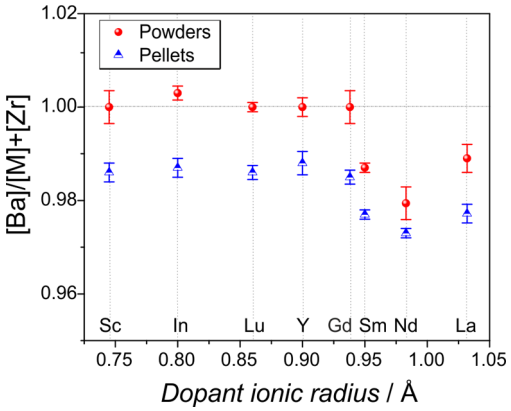

Figure 6. Barium content as a function of the dopant ionic radius in powders (circles) and pellets (triangles) BZ-M.

function of the ionic radii of the dopants, for both powders and pellets. The Ba content in the case of the powders was close to the theoretical value for all the dopants with ionic radius smaller than Sm, while for Sm, Nd, and La, the measured Ba content was smaller than the theoretical value, which supports the hypothesis of dopant incorporation into the Ba site, with consequent Ba losses.

In the pellets, the measured Ba concentration was lower than in the respective powders, regardless of the ionic radius of the dopant, due to the unavoidable Ba loss that occurs during the high temperature sintering process.

Chemical analysis (not shown here) confirmed also that the dopant content was close to the nominal value for all samples. Only In- and La-doped sintered samples showed a dopant content smaller than the nominal value (0.16 and 0.17, respectively).

Electrical Conductivity. Figure 7a reports the Arrhenius plots of the BZ-M bulk conductivity in humidified atmosphere. The highest conductivity values were observed for Y-, Gd-, Tm-, and Lu-doped barium zirconate pellets. The bulk conductivity values measured for BZ-Y (3×10^{-5} S cm^{-1} at 100 °C) are comparable to literature data.[33,46] For sake of comparison, Figure 7a also reports the bulk conductivity of undoped barium zirconate. Only La- and Al-doped barium zirconate showed conductivity values lower than the undoped barium zirconate, as revealed by the XRD analysis shown in Figure 3, parts a and j; both contain secondary phases. This suggests that the secondary phases hinder the proton migration.

Figure 7b shows the Arrhenius plot of the specific grain boundary conductivities in humidified argon for BZ-M sintered pellets, which as expected are much lower (3 orders of magnitude at 350 °C) than the bulk conductivity for all compositions. The specific grain boundary conductivity of the compositions studied showed a maximum variation of 2 orders of magnitude in the temperature range studied, which indicates that this property is less affected by the choice of the dopant compared to the bulk migration process.

The Arrhenius plot of the total conductivity, which is of critical importance for practical applications, is shown in Figure 7c. This property depends not only on the conductivity of the material but also on morphological properties such as the sinterability and grain dimensions.

To better understand the influence of the dopant on the ionic transport, the bulk conductivity at 110 °C and the activation energy of the bulk conductivity are plotted as a function of the dopant ionic radius in Figure 8a, excluding here La and Al as dopants. It is noteworthy that the choice of the dopant can change the conductivity in a range of 4 orders of magnitude. The highest values of bulk conductivity have been measured for yttrium- and thulium-doped barium zirconate. Similar bulk conductivities were also observed for Gd and Lu as dopants, which indeed have an ionic radius very close to Y and Tm. Bulk conductivities about 1 order of magnitude smaller were observed for the smaller dopants, i.e., Sc and In, while a drastic drop was observed for the larger cations (Sm and Nd). Also the activation energy for the bulk migration process showed a dependence on the dopant ionic radii, achieving the lowest values for dopants with ionic radius between Lu and Gd

DOI: 10.1021/acs.jpcc.7b02163
J. Phys. Chem. C 2017, 121, 9739−9747

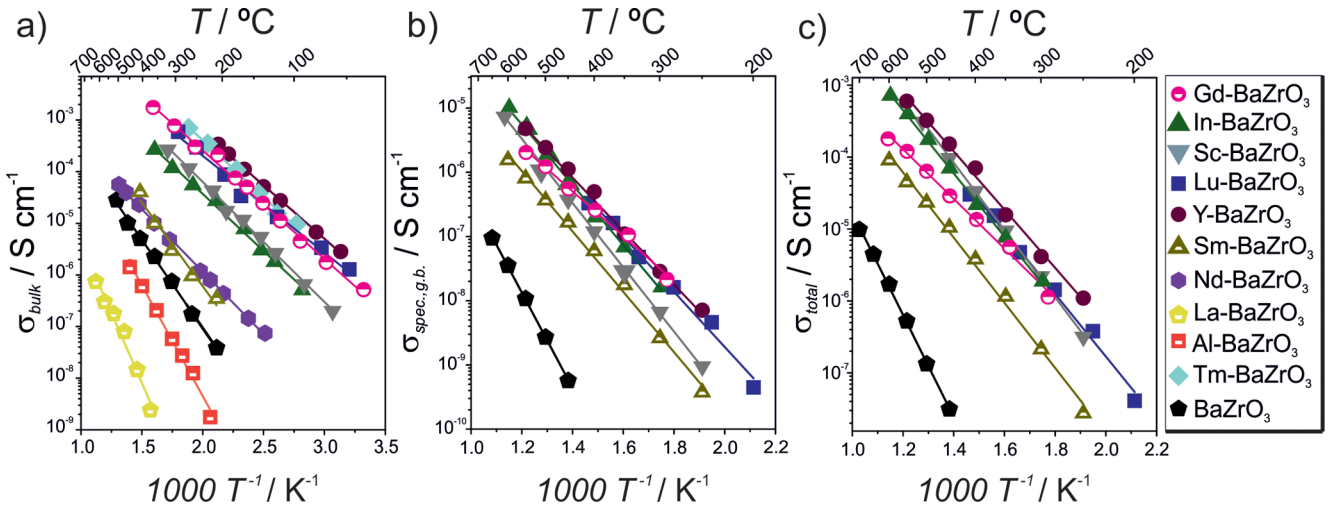

Figure 7. Temperature dependence of the conductivity in humidified (3% H_2O) Ar of BZ-M with different dopants: (a) bulk conductivity, (b) specific grain boundary conductivity, and (c) total conductivity.

(from 0.40 to 0.45 eV), and the highest values of 0.67 eV for Nd.

Our experimental results indeed confirm recent theoretical works reported in the literature where the effect of the dopant ionic size on the mobility and stability of protonic defects in different perovskites (zirconates, stannates, cerates) was studied by first principle density functional theory calculations.[47−49] These studies pointed out that the energy landscape felt by the proton is strongly affected by the ionic radius of the dopant: for small dopant ionic radii the proton is mainly stabilized when bonded to an oxygen first neighbor of the dopant, while for large ionic radii the most stable position is bonded to an oxygen second neighbor of the dopant. Consistently the stability of the proton in the first neighbor position decreases increasing the dopant ionic radii, while the stability in the second neighbor position follows the opposite trend. The total association energy of the proton with the dopant results therefore from the difference between the stabilization energy in the two different positions.

In the aforementioned studies similar dopants, as those used in the present work, were considered: Ga, Sc, In, Y, and Gd, together with Er for the cerates[49] and La for the stannates.[48] The value of the optimal dopant ionic radius depends on the size of the host cation (Zr, Sn and Ce), nevertheless in all cases the trapping energy reaches a minimum for dopants with radius significantly larger than the host cation, generally close to Y and Gd. This means that doping with cations with ionic radius close to these two elements leads to the lowest proton trapping, while for larger or smaller radii the proton trapping increases.

Stokes et al.,[50] using a different computational approach suggested a similar trend of the trapping energy as a function of the ionic radius, reaching a minimum value for Gd, however they considered the proton bonded only to the oxygen first neighbor of the dopant.

The effect of the proton-dopant association on the activation energy has been computed for $BaZrO_3$ by Björketun et al.,[47] the values estimated are in agreement with those reported in the present work considering the experimental uncertainty, especially for dopant ionic radii close to Y. In particular their study suggests that the minimum in the proton-dopant association energy for doped barium zirconates occurs for Y dopant.

In the present work the minimum in the activation energy corresponds to Lu as dopant, while in the results reported by Han et al.[29] corresponds to Tm-doped barium zirconate. This suggests that the minimum in the trapping energy in doped barium zirconates occurs for dopant with ionic radii close to that of Y, but slightly smaller. Trapping energies and activation energies for these values of dopant ionic radii have indeed not been calculated.

Even though the effect on the conductivity has not been computed, it is reasonable to expect a trend opposite to that of the trapping energy: dopants with lower proton-dopant association energy should lead to higher conductivity. The conductivity therefore is expected to increase with increasing the dopant ionic radius toward Y and to decrease for larger dopants, in agreement with our experimental results.

Additionally for Sm and Nd the large ionic radius leads to a partial substitution on the Ba site which decreases the total concentration of oxygen vacancies resulting in a lower incorporation of charge carriers.

As mentioned before, also for BZ-Gd, it is reasonable to expect a certain degree of substitution on the Ba site, which is supported also by the analysis of the lattice parameter from XRD. In this case the enhancement of the conductivity due to the low association between proton and dopant would be reduced by the effect of the Gd substitution on the Ba site, which would decrease the concentration of charge carriers.

As shown in Figure 8b, the grain boundary conductivities are not significantly influenced by the ionic radii of the dopant, and only slightly decrease for dopant ionic radius larger than Y. The activation energies are higher than the respective bulk activation energies (Figure 8a) and in agreement with values reported in literature for comparable doping levels.[6,37,51]

The total conductivity is also not strongly affected by the ionic radius of the dopant as reported in Figure 8c; it slightly decreases for dopants with ionic radii larger than Lu, even though the values do not vary more than 1 order of magnitude. The activation energies show as well a small variation increasing the dopant ionic radius.

From the comparison of the different properties investigated in this study Gd-BZ appears particularly promising for practical application as proton conducting electrolyte in fuel cells. Indeed it shows an high bulk conductivity, originating from a

DOI: 10.1021/acs.jpcc.7b02163
J. Phys. Chem. C 2017, 121, 9739−9747

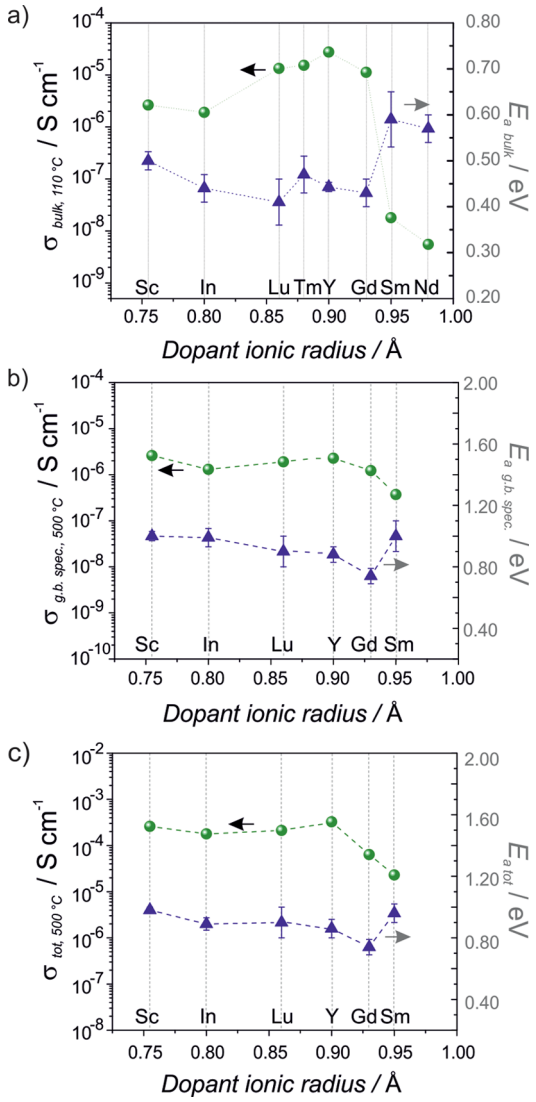

Figure 8. Conductivities and activation energies measured in humidified 3% vol H_2O − Ar of BZ-M doped with different cations. (a) Bulk conductivity at 110 °C and activation energies. (b) Grain boundaries specific conductivity at 500 °C and activation energies. (c) Total conductivity at 500 °C and activation energies. Error bars reported indicate the 95% confidence intervals.

weak trapping effect of Gd on the protons and a grain boundary conductivity which is comparable to the values measured for other dopants. The total conductivity is comparable to the conductivities of barium zirconate doped with other acceptor dopants (In, Sc, Lu), while it has a significantly lower activation energy. Furthermore, Gd-doped barium zirconate reveals better morphological properties since the good sinterability results in the formation of dense samples with large grains. The comprehensive comparison of several materials properties reported in the present study suggests that Gd-BZ may deserve further investigation for the optimization of the doping content and the sintering procedure. The better sinterability of Gd-BZ compared to other doped BZ with similar conductivity, can favor its use as gastight electrolyte in SOFCs. Moreover, computational results indicated Gd as one of the dopants with the smallest trapping effect,[47,49] which further suggests that Gd-BZ could improve its performance upon optimization of the synthesis procedure, sintering and dopant content.

CONCLUSIONS

In this study the effect of different dopants, i.e., Al, Sc, In, Lu, Tm, Y, Gd, Sm, Nd, and La on the structural, sintering and electrical properties of 20 mol % doped $BaZrO_3$ was investigated.

Overall we observed that the sinterability improves varying the dopant cationic radii from Sc to Nd and also the shrinkage increases sensibly increasing the ionic radii of the dopants. The highest shrinkages of doped barium zirconate were measured for Sm, Nd, and La as dopants. These form ceramic pellets with dense microstructure and average grain sizes between 4 and 8 μm. A linear relation between the dopant ionic radius and the lattice parameter of the compound was found for the elements between Sc and Y, while dopants with ionic radii larger than Gd showed the tendency to substitute Ba instead of Zr.

Lu-, Tm-, Y-, and Gd-doped barium zirconate exhibit the highest bulk conductivity and the lowest activation energy among the studied compositions, in agreement with computational studies on doped barium zirconate and similar perovskites. Dopants with ionic radii larger than Gd show much lower conductivity, due to their partial substitution on the Ba site.

It is worth noticing that mainly the bulk conductivity is affected by the dopant ionic radii, while only a slight influence was observed on the grain boundary conductivity.

Overall, the present study illustrates the critical role of the dopant element in modifying the stability, sinterability, and proton conductivity of barium zirconate. Our investigations show that high bulk conductivity can be obtained for a variety of dopants, i.e., Tm, Lu, Y, and Gd. When the sinterability and grain boundary density are taken into account, the best dopant appears to be Gd.

Yttrium-doped barium zirconate and thulium-doped barium zirconate showed the highest proton conductivity among the studied composition; in addition Gd also appears as a promising dopant that brings to both high ionic conductivity and good morphological properties.

Indeed, the good sinterability of Gd-BZO allows producing dense samples with relatively large grain size, minimizing the total grain boundary conductivity without hampering the bulk conductivity. The result is a doped BZO with good morphological properties (dense electrolytes are needed in fuel cells to avoid gas crossover) and high total conductivity. Therefore, on the basis of our methodological investigations we proposed Gd-BZO as a novel potential proton conducting electrolyte for low temperature SOFC.

AUTHOR INFORMATION

Corresponding Authors

*(D.P.) Telephone: +41 56 310 42 67. E-mail: daniele.pergolesi@psi.ch.

*(E.T.) E-mail: traversa@uniroma2.it. Telephone: +39 06 7259 4492.

ORCID

Elisa Gilardi: 0000-0002-8831-0104

Author Contributions

The manuscript was written through contributions of all authors. All authors have given approval to the final version of the manuscript.

Notes

The authors declare no competing financial interest.

DOI: 10.1021/acs.jpcc.7b02163
J. Phys. Chem. C 2017, 121, 9739−9747

■ ACKNOWLEDGMENTS

This research was supported by the NCCR MARVEL, funded by the Swiss National Science Foundation.

■ REFERENCES

(1) Malavasi, L.; Fisher, C. A. J.; Islam, M. S. Oxide-Ion and Proton Conducting Electrolyte Materials for Clean Energy Applications: Structural and Mechanistic Features. *Chem. Soc. Rev.* **2010**, *39*, 4370−4387.

(2) Shi, Y. U.; Bork, A. H.; Schweiger, S.; Rupp, J. L. M. The Effect of Mechanical Twisting on Oxygen Ionic Transport in Solid-State Energy Conversion Membranes. *Nat. Mater.* **2015**, *14*, 721−728.

(3) Evans, A.; Bieberle-Hutter, A.; Rupp, J. L. M.; Gauckler, L. J. Review on Microfabricated Micro-Solid Oxide Fuel Cell Membranes. *J. Power Sources* **2009**, *194*, 119−129.

(4) Iwahara, H.; Yajima, T.; Hibino, T.; Ushida, H. Performace of Solid Oxide Fuel-Cell Using Proton and Oxide-Ion Mixed Conductors Based on $BaCe_{1-x}Sm_xO_{3-\alpha}$. *J. Electrochem. Soc.* **1993**, *140*, 1687−1691.

(5) Pergolesi, D.; Fabbri, E.; D'Epifanio, A.; Di Bartolomeo, E.; Tebano, A.; Sanna, S.; Licoccia, S.; Balestrino, G.; Traversa, E. High Proton Conduction in Grain-Boundary-Free Yttrium-Doped Barium Zirconate Films Grown by Pulsed Laser Deposition. *Nat. Mater.* **2010**, *9*, 846−852.

(6) Yamazaki, Y.; Hernandez-Sanchez, R.; Haile, S. M. High Total Proton Conductivity in Large-Grained Yttrium-Doped Barium Zirconate. *Chem. Mater.* **2009**, *21*, 2755−2762.

(7) Kreuer, K. D. Proton-Conducting Oxides. *Annu. Rev. Mater. Res.* **2003**, *33*, 333−359.

(8) Fabbri, E.; Pergolesi, D.; Traversa, E. Materials Challenges Toward Proton-Conducting Oxide Fuel Cells: A Critical Review. *Chem. Soc. Rev.* **2010**, *39*, 4355−4369.

(9) Fabbri, E.; Pergolesi, D.; Licoccia, S.; Traversa, E. Does the Increase in Y-Dopant Concentration Improve the Proton Conductivity of $BaZr_{1-x}Y_xO_{3-\delta}$ Fuel Cell Electrolytes? *Solid State Ionics* **2010**, *181*, 1043−1051.

(10) Messerschmitt, F.; Kubicek, M.; Rupp, J. L. M. How Does Moisture Affect the Physical Property of Memristance for Anionic-Electronic Resistive Switching Memories? *Adv. Funct. Mater.* **2015**, *25*, 5117−5125.

(11) Nowick, A. S.; Du, Y. High-Temperature Protonic Conductors with Perovskite-Related Structures. *Solid State Ionics* **1995**, *77*, 137−146.

(12) Fabbri, E.; Bi, L.; Pergolesi, D.; Traversa, E. Towards the Next Generation of Solid Oxide Fuel Cells Operating Below 600 °C with Chemically Stable Proton-Conducting Electrolytes. *Adv. Mater.* **2012**, *24*, 195−208.

(13) Fabbri, E.; Pergolesi, D.; Licoccia, S.; Traversa, E. Does the Increase in Y-Dopant Concentration Improve the Proton Conductivity of $BaZr_{1-x}Y_xO_{3-\delta}$ Fuel Cell Electrolytes? *Solid State Ionics* **2010**, *181*, 1043−1051.

(14) Yamazaki, Y.; Hernandez-Sanchez, R.; Haile, S. M. Cation Non-Stoichiometry in Yttrium-Doped Barium Zirconate: Phase Behavior, Microstructure and Proton Conductivity. *J. Mater. Chem.* **2010**, *20*, 8158−8166.

(15) Yamazaki, Y.; Yang, C. K.; Haile, S. M. Unraveling the Defect Chemistry and Proton Uptake of Yttrium-Doped Barium Zirconate. *Scr. Mater.* **2011**, *65*, 102−107.

(16) Norby, T.; Widerøe, M.; Glockner, R.; Larring, Y. Hydrogen in Oxides. *Dalton Trans.* **2004**, 3012−3018.

(17) Giannici, F.; Longo, A.; Balerna, A.; Kreuer, K. D.; Martorana, A. Proton Dynamics in In:$BaZrO_3$: Insights on the Atomic and Electronic Structure from X-ray Absorption Spectroscopy. *Chem. Mater.* **2009**, *21*, 2641−2649.

(18) Karlsson, M.; Matic, A.; Knee, C. S.; Ahmed, I.; Eriksson, S. G.; Borjesson, L. Short-Range Structure of Proton-Conducting Perovskite $BaIn_xZr_{1-x}O_{3-x/2}$ (x = 0−0.75). *Chem. Mater.* **2008**, *20*, 3480−3486.

(19) Giannici, F.; Longo, A.; Kreuer, K. D.; Balerna, A.; Martorana, A. Dopants and Defects: Local Structure and Dynamics in Barium Cerates and Zirconates. *Solid State Ionics* **2010**, *181*, 122−125.

(20) Chen, Q. L.; Braun, A.; Ovalle, A.; Savaniu, C. D.; Graule, T.; Bagdassarov, N. Hydrostatic Pressure Decreases the Proton Mobility in the Hydrated $BaZr_{0.9}Y_{0.1}O_3$ Proton Conductor. *Appl. Phys. Lett.* **2010**, *97*, 041902.

(21) Chen, Q. L.; Braun, A.; Yoon, S.; Bagdassarov, N.; Graule, T. Effect of Lattice Volume and Compressive Strain on the Conductivity of BaCeY-oxide Ceramic Proton Conductors. *J. Eur. Ceram. Soc.* **2011**, *31*, 2657−2661.

(22) van Duin, A. C. T.; Merinov, B. V.; Han, S. S.; Dorso, C. O.; Goddard, W. A. ReaxFF Reactive Force Field for the Y-Doped $BaZrO_3$ Proton Conductor with Applications to Diffusion Rates for Multi-granular Systems. *J. Phys. Chem. A* **2008**, *112*, 11414−11422.

(23) Merinov, B.; Goddard, W. A. Proton Diffusion Pathways and Rates in Y-doped $BaZrO_3$ Solid Oxide Electrolyte from Quantum Mechanics. *J. Chem. Phys.* **2009**, *130*, 194707.

(24) Gomez, M. A.; Chunduru, M.; Chigweshe, L.; Foster, L.; Fensin, S. J.; Fletcher, K. M.; Fernandez, L. E. The Effect of Yttrium Dopant on the Proton Conduction Pathways of $BaZrO_3$, a Cubic Perovskite. *J. Chem. Phys.* **2010**, *132*, 214709.

(25) Samgin, A. L. Lattice-Assisted Proton Motion in Perovskite Oxides. *Solid State Ionics* **2000**, *136-137*, 291−295.

(26) Islam, M. S.; Davies, R. A.; Gale, J. D. Proton Migration and Defect Interactions in the $CaZrO_3$ Orthorhombic Perovskite: A Quantum Mechanical Study. *Chem. Mater.* **2001**, *13*, 2049−2055.

(27) Kreuer, K. D.; Adams, S.; Munch, W.; Fuchs, A.; Klock, U.; Maier, J. Proton Conducting Alkaline Earth Zirconates and Titanates for High Drain Electrochemical Applications. *Solid State Ionics* **2001**, *145*, 295−306.

(28) Han, D. L.; Hatada, N.; Uda, T. Chemical Expansion of Yttrium-Doped Barium Zirconate and Correlation with Proton Concentration and Conductivity. *J. Am. Ceram. Soc.* **2016**, *99*, 3745−3753.

(29) Han, D. L.; Shinoda, K.; Sato, S.; Majima, M.; Uda, T. Correlation Between Electroconductive and Structural Properties of Proton Conductive Acceptor-Doped Barium Zirconate. *J. Mater. Chem. A* **2015**, *3*, 1243−1250.

(30) Gorelov, V. P.; Balakireva, V. B.; Kleshchev, Y. N.; Brusentsov, V. P. Preparation and Electrical Conductivity of $BaZr_{1-x}R_xO_{3-\alpha}$ (R = Sc, Y, Ho, Dy, Gd, In). *Inorg. Mater.* **2001**, *37*, 535−538.

(31) Yamazaki, Y.; Blanc, F.; Okuyama, Y.; Buannic, L.; Lucio-Vega, J. C.; Grey, C. P.; Haile, S. M. Proton Trapping in Yttrium-Doped Barium Zirconate. *Nat. Mater.* **2013**, *12*, 647−651.

(32) Iwahara, H.; Yajima, T.; Hibino, T.; Ozaki, K.; Suzuki, H. Protonic Conduction in Calcium, Strontium and Barium Zirconates. *Solid State Ionics* **1993**, *61*, 65−69.

(33) Imashuku, S.; Uda, T.; Nose, Y.; Taniguchi, G.; Ito, Y.; Awakura, Y. Dependence of Dopant Cations on Microstructure and Proton Conductivity of Barium Zirconate. *J. Electrochem. Soc.* **2009**, *156*, B1−B8.

(34) Laidoudi, M.; Talib, I. A.; Omar, R. Investigation of the Bulk Conductivity of $BaZr_{0.95}M_{0.05}O_3$ (M = Al, Er, Ho, Tm, Yb and Y) Under Wet N_2. *J. Phys. D: Appl. Phys.* **2002**, *35*, 397−401.

(35) Han, D. L.; Hatada, N.; Uda, T. Microstructure, Proton Concentration and Proton Conductivity of Barium Zirconate Doped with Ho, Er, Tm and Yb. *J. Electrochem. Soc.* **2016**, *163*, F470−F476.

(36) Imashuku, S.; Uda, T.; Nose, Y.; Awakura, Y. Fabrication and Electrical Characterization of 15% Yttrium-Doped Barium Zirconate-Nitrate Freeze Drying Method Combined with Vacuum Heating. *J. Alloys Compd.* **2011**, *509*, 3872−3879.

(37) Chen, C.-T.; Danel, C. E.; Kim, S. On the Origin of the Blocking Effect of Grain-Boundaries on Proton Transport in Yttrium-Doped Barium Zirconates. *J. Mater. Chem.* **2011**, *21*, 5435−5442.

(38) Bonanos, N.; Knight, K. S.; Ellis, B. Perovkite Solid Electrolytes - Structure, Transport-Properties and Fuel-Cell Applications. *Solid State Ionics* **1995**, *79*, 161−170.

DOI: 10.1021/acs.jpcc.7b02163
J. Phys. Chem. C 2017, 121, 9739−9747

(39) Shima, D.; Haile, S. M. The Influence of Cation non-Stoichiometry on the Properties of Undoped and Gadolinia-Doped Barium Cerate. *Solid State Ionics* **1997**, *97*, 443−455.
(40) Haile, S. M.; Staneff, G.; Ryu, K. H. Non-Stoichiometry, Grain Boundary Transport and Chemical Stability of Proton Conducting Perovskites. *J. Mater. Sci.* **2001**, *36*, 1149−1160.
(41) Wu, J.; Li, L. P.; Espinosa, W. T. P.; Haile, S. T. Defect Chemistry and Transport Properties of $Ba_xCe_{0.85}M_{0.15}O_{3-\delta}$. *J. Mater. Res.* **2004**, *19*, 2366−2376.
(42) Islam, M. S.; Slater, P. R.; Tolchard, J. R.; Dinges, T. Doping and Defect Association in $AZrO_3$ (A = Ca, Ba) and $LaMO_3$ (M = Sc, Ga) Perovskite-Type Ionic Conductors. *Dalton Trans.* **2004**, 3061−3066.
(43) Brauer, G.; Kristen, H. Oxygen Perovskites with Tetravalent Neodymium. *Z. Anorg. Allg. Chem.* **1979**, *456*, 41−53.
(44) Oishi, M.; Yashiro, K.; Sato, K.; Mizusaki, J.; Kitamura, N.; Amezawa, K.; Kawada, T.; Uchimoto, Y. Oxygen nonstoichiometry of the perovskite-type oxides $BaCe_{0.9}M_{0.1}O_{3-\delta}$ (M = Y, Yb, Sm, Tb, and Nd). *Solid State Ionics* **2008**, *179*, 529−535.
(45) Periercamby, L.; Thomas, G. Ssolid Way Synthesis of Barium Aluminate. Kinetic Study of the Formation of Intermediate Compounds. *Solid State Ionics* **1993**, *63*−*65*, 128−135.
(46) Kreuer, K. D. On the Complexity of Proton Conduction Phenomena. *Solid State Ionics* **2000**, *136-137*, 149−160.
(47) Bjorketun, M. E.; Sundell, P. G.; Wahnstrom, G. Effect of Acceptor Dopants on the Proton Mobility in $BaZrO_3$: A Density Functional Investigation. *Phys. Rev. B: Condens. Matter Mater. Phys.* **2007**, *76*, 054307.
(48) Bevillon, E.; Hermet, J.; Dezanneau, G.; Geneste, G. How Dopant Size Influences the Protonic Energy Landscape in $BaSn_{1-x}M_xO_{3-x/2}$ (M = Ga, Sc, In, Y, Gd, La). *J. Mater. Chem. A* **2014**, *2*, 460−471.
(49) Loken, A.; Bjorheim, T. S.; Haugsrud, R. The Pivotal Role of the Dopant Choice on the Thermodynamics of Hydration and Associations in Proton Conducting $BaCe_{0.9}X_{0.1}O_{3-\delta}$ (X = Sc, Ga, Y, In, Gd and Er). *J. Mater. Chem. A* **2015**, *3*, 23289−23298.
(50) Stokes, S. J.; Islam, M. S. Defect Chemistry and Proton-Dopant Association in $BaZrO_3$ and $BaPrO_3$. *J. Mater. Chem.* **2010**, *20*, 6258−6264.
(51) Cervera, R. B.; Oyama, Y.; Miyoshi, S.; Oikawa, I.; Takamura, H.; Yamaguchi, S. Nanograined Sc-Doped $BaZrO_3$ as a Proton Conducting Solid Electrolyte for Intermediate Temperature Solid Oxide Fuel Cells (IT-SOFCs). *Solid State Ionics* **2014**, *264*, 1−6.

DOI: 10.1021/acs.jpcc.7b02163
J. Phys. Chem. C 2017, 121, 9739−9747